Reconfigurable self-assembly through chiral control of interfacial tension

Thomas Gibaud[1], Edward Barry[1], Mark J. Zakhary[1], Mir Henglin[1], Andrew Ward[1], Yasheng Yang[1], Cristina Berciu[2], Rudolf Oldenbourg[3], Michael F. Hagan[1], Daniela Nicastro[2], Robert B. Meyer[1] and Zvonimir Dogic[1]

[1]The Martin Fisher School of Physics, Brandeis University, 415 South St., Waltham, MA 02454, USA

[2]Department of Biology, Brandeis University, 415 South St., Waltham, MA 02454, USA

[3]Marine Biological Laboratory, 7 MBL St., Woods Hole, MA 02543, USA

From determining optical properties of simple molecular crystals to establishing preferred handedness in highly complex vertebrates, molecular chirality profoundly influences the structural, mechanical, and optical properties of both synthetic and biological matter at macroscopic lengthscales[1,2]. In soft materials such as amphiphilic lipids and liquid crystals, the competition between local chiral interactions and global constraints imposed by the geometry of the self-assembled structures leads to frustration and the assembly of unique materials[3-6]. An example of particular interest is smectic liquid crystals, where the 2D layered geometry cannot support twist, expelling chirality to the edges in a manner analogous to the expulsion of a magnetic field from superconductors[7-10]. Here, we demonstrate a previously unexplored consequence of this geometric frustration which leads to a new design principle for the assembly of chiral molecules. Using a model system of colloidal membranes[11], we show that molecular chirality can control the interfacial tension,

an important property of multi-component mixtures. This finding suggests an analogy between chiral twist which is expelled to the edge of 2D membranes, and amphiphilic surfactants which are expelled to oil-water interfaces[12]. Similar to surfactants, chiral control of interfacial tension drives the assembly of myriad polymorphic assemblages such as twisted ribbons with linear and circular topologies, starfish membranes, and double and triple helices. Tuning molecular chirality *in situ* enables dynamical control of line tension that powers polymorphic transitions between various chiral structures. These findings outline a general strategy for the assembly of reconfigurable chiral materials which can easily be moved, stretched, attached to one another, and transformed between multiple conformational states, thus enabling precise assembly and nano-sculpting of highly dynamical and designable materials with complex topologies.

For experiments on chiral self-assembly, we used a two-component mixture consisting of 880 nm long rod-like *fd* viruses and the non-adsorbing polymer Dextran. In aqueous suspension, *fd* viruses alone exhibit purely repulsive interactions[13]. Adding non-adsorbing polymer to a dilute isotropic suspension of *fd* rods induces attractive interactions via the depletion mechanism and leads to their condensation into colloidal membranes, equilibrium structures consisting of one-rod-length thick liquid-like monolayers of aligned rods (Fig. 1a)[11]. Despite having different structures on molecular lengthscales, the long-wavelength coarse-grained properties of colloidal membranes are identical to those of conventional lipid bilayers. However, unlike their amphiphilic counterparts, colloidal membranes do not form vesicles and are instead observed as freely suspended disks with exposed edges. Here, we investigate the behavior of these exposed edges in a manner analogous to previously studied liquid-liquid domains embedded in lipid bilayers[14-16]. For our experiments, it is essential that *fd* viruses are chiral, i.e. a pair of aligned viruses minimizes their interaction energy when they are slightly twisted in a preferred direction with respect to each other. The strength of chiral interactions can be continuously tuned to zero through either genetic or physical methods (Supplementary Fig. 1) [13,17].

Before investigating chiral membranes, we determined the structure of a membrane's edge composed of simpler achiral rods using three complimentary imaging techniques, namely 2D and 3D polarization microscopy and electron microscopy. The local tilting of the rods within a membrane was determined using 2D LC-PolScope, which produces images in which the intensity of each pixel represents the local retardance of the membrane (Fig. 1d)[18]. Such images can be quantitatively related to the tilting of the rods away from the layer normal, the z-axis[19]. Rods in the bulk of a membrane are aligned along the z-axis, so that 2D LC-PolScope images appear black in that region (Fig. 1e). In contrast, the bright birefringent ring along the membrane's periphery reveals local tilting of the rods (Fig. 1e, Supplementary Fig. 2). For achiral rods, this indicates that a membrane has a hemi-toroidal curved edge (Fig. 1b, c). In comparison to an untilted edge, a curved edge structure lowers the area of the rod/polymer interface, thus reducing interfacial tension, at the cost of increasing the elastic energy due to twist distortion. This hypothesis is confirmed by visualizing the 3D membrane structure using electron tomography, which shows that the viruses' long axis transitions from being parallel to the z-axis in the membrane bulk to perpendicular to the z-axis and tangent to the edge along the membrane periphery (Fig. 1d, Supplementary Fig. 3). For achiral viruses, the spontaneous twist at the edges is equally likely to be clockwise or counter-clockwise. However, the 2D LC-PolScope records only 2D projections of the birefringence map and thus cannot distinguish between these two possibilities. For this reason we used 3D-LC-PolScope[20], which reveals that achiral rods are equally likely to tilt in either direction, thus confirming the spontaneously broken chiral symmetry at the edge of an achiral membrane (Fig. 1f-h, Supplementary Fig. 4). Simulations of hard achiral spherocylinders and depletant molecules provide additional verification that interfacial effects alone cause spontaneous twisting of achiral rods at the membrane's edge (Supplementary Fig. 5).

When viewed with optical microscopy, a membrane's edge exhibits significant thermal fluctuations, the analysis of which yields the line tension γ_{eff}, the energetic cost required to move rods from the membrane interior to the periphery[11,21,22] (Fig. 2a). A typical fluctuation spectrum for an achiral edge is shown in Fig. 2b. In the low-q regime, the mean square Fourier amplitudes $\langle a^2_q \rangle$ are independent of the wave vector q, allowing us to extract the effective line tension $\gamma_{eff} = k_bT/\langle a^2_q \rangle$[11]. In the large-$q$ limit, fluctuations are significantly suppressed when compared to those of a simple interface, scaling as $1/q^2$. One possible

explanation is that fluctuations are suppressed due to a quasi-1D nematic phase at the edge, which is a direct consequence of rod tilting (Fig. 1e). At large wavelengths, the elastic energy of deforming the quasi-1D nematic phase is negligible and the fluctuations are dominated by the line tension. With decreasing wavelength there is an increasing energetic penalty associated with bending the quasi-1D nematic, resulting in the suppression of fluctuations at those wavelengths.

Next, we demonstrated that the chirality of the constituent rods controls the magnitude of γ_{eff}. The global constraints imposed by the 2D membrane topology are fundamentally incompatible with local twisting (chiral interactions) between constituent rods, leading to the expulsion of chirality (untwisting of rods) from the bulk of the membrane[7]. It follows that introducing chirality raises the energy of rods in the membrane bulk, while simultaneously lowering the energy of rods close to the edge, where they are free to twist and satisfy chiral interactions. Therefore, we hypothesize that there are two contributions to the effective line tension: $\gamma_{eff} = \gamma_{bare}-\gamma_{chiral}$, where γ_{bare} is the line tension of a membrane's edge composed of achiral rods, and γ_{chiral} is the chiral contribution to the line tension[19,23]. To independently measure γ_{bare} and γ_{chiral}, we utilized the temperature dependence of *fd* chirality (Supplementary Fig.1). γ_{bare} was measured at high temperature (60^{o}C) where rods are achiral (γ_{chiral}=0) and therefore γ_{eff}=γ_{bare} (Fig. 2c). Decreasing temperature increases the strength of chiral interactions, resulting in a smaller γ_{eff} and demonstrating that chirality indeed reduces line tension (Fig. 2c). Temperature dependent chiral contributions ($\gamma_{chiral}(T)$=-$\gamma_{eff}(T)$+γ_{bare}) were converted into a function that depends on the chiral wavevector q_0 using measurements of the temperature dependence on the cholesteric twist (Supplementary Fig. 1). Importantly, γ_{chiral} measured at different depletant concentrations collapse onto a universal curve (Fig. 2d), confirming that the two contributions to γ_{eff} are uncorrelated. Our data shows that chirality can reduce the line tension by as much as 450 k_BT/μm (Fig. 2d). To independently test this hypothesis, γ_{eff} was measured for membranes composed of the mutant *fd* Y21M. In contrast to *fd wt*, the chirality of *fd* Y21M is temperature-independent (Supplementary Fig. 6). We find that γ_{eff} for *fd* Y21M membranes is temperature independent over the entire measurement range, unambiguously demonstrating chiral control of line tension and ruling out any intrinsic temperature effects.

Our findings raise the intriguing possibility that at sufficiently low temperatures, the chiral contribution to interfacial energy could dominate the bare line tension, lowering the energetic cost of creating edges and leading to their spontaneous formation. In this respect, we expect chirality to play a role similar to amphiphilic surfactants in oil/water mixtures, which lower surface tension and lead to the formation of excess interfaces through the assembly of microemulsions. To investigate this possibility, we quenched a membrane assembled at low depletant (Dextran) concentration from the high temperature achiral phase. With decreasing temperature, fluctuations of the membrane edge become more pronounced, indicating decreasing γ_{eff}. Eventually, the edge becomes unstable, resulting in a remarkable polymorphic transition in which twisted ribbon-like structures grow along the entire periphery of the disk, generating a starfish-shaped membrane (Fig. 3a, Supplementary Movie 1). This polymorphic transition is reversible; with increasing temperature the starfish membrane collapses back into a 2D disk. The stability diagram indicates that 1D twisted ribbons are stable at low Dextran concentrations and low temperatures (small γ_{bare} and large γ_{chiral}), while flat 2D membranes are stable for large γ_{bare} or small γ_{chiral} (Fig. 3b). DIC microscopy reveals the overall structure of the ribbons, such as their pitch and width (Fig. 3a); fluorescence microscopy uncovers the liquid-like dynamics of single rods within the assemblage (Fig. 3c, Supplementary Movie 2); and 2D-LC-PolScope quantitatively determines the local tilt of the rods (Fig. 3d). A schematic representation of the twisted ribbons based on this information, indicating inhomogeneous tilting of the rods within a ribbon, is shown in Fig. 3e. Such data is in agreement with recent theoretical predictions[24].

Chiral self-assembly produces structures which combine seemingly divergent properties of high elasticity and fluidity. To demonstrate these properties, we trapped two opposite sides of a flat disk with a dual-beam optical trap and applied an extensional force, causing the transition from a stretched disk into a twisted ribbon (Fig. 3f, Supplementary Movie 3). This mechanically induced disk-to-ribbon transition is reversible; upon removing the optical trap the highly elastic ribbon relaxes back into its original shape. Furthermore, using optical tweezers it is possible to systematically change the architecture of the chiral assemblages, enabling new pathways for assembling nanomaterials with highly complex topologies. For example, two ends of a linear twisted ribbon are easily joined together to assemble a closed ring-like polymeric structure. The disk-to-ribbon transition is tightly coupled to the assemblage topology (Fig. 4d).

Upon increasing the temperature, all linear ribbons transition into achiral disks (Supplementary Movie 4), while closed ring-like ribbons remain twisted due to the constraint imposed by the ring topology (Supplementary Movie 5).

The chiral assembly pathways described here are hierarchical, opening up the possibility that simple changes on microscopic (Angstrom) lengthscales can be used to control structures on macroscopic (millimeter) lengthscales[25,26]. At the smallest relevant lengthscale, each virus is assembled from DNA which is coated with thousands of copies of the major coat protein. At the mesoscopic lengthscale, attractive depletion interactions condense dilute rod-like viruses into self-limited metastable mesoscopic colloidal disks whose diameter is approximately one twist penetration length (Fig. 4a)[19,23,27,28]. Once assembled, mesoscopic disks themselves experience mutual attractions, resulting in lateral coalescence and formation of twisted doublets. On longer timescales this coalescence process continues, producing ribbons with complex topologies and multiple branching points (Supplementary Fig. 7). The length of these ribbons can reach macroscopic (millimeter) dimensions. This hierarchical assembly process describes a robust synthesis of ribbons that behave as supra-molecular polymers and can assemble into even more complex structures at higher levels of hierarchy, such as toroids (Fig. 4b). Under certain conditions, ribbons also wrap around each other in order to build a myriad of double and triple helical structures (Fig. 4c, Supplementary Fig. 8). A challenge associated with hierarchical assembly pathways is to control the final macroscopic assemblage by specific modification of relevant microscopic parameters. Previous work showed that even a single amino acid mutation of the major coat protein can alter the microscopic chirality of individual viruses[13]. We used this finding to demonstrate that such amino acid exchange propagates across all hierarchical levels, switching the ribbon handedness and allowing for microscopic control of macroscopic ribbon chirality (Fig. 4e, f).

In conclusion, we have shown that the chirality of the constituent molecules can be used to tune the interfacial tension, an important property of complex soft materials. The potential of hierarchical chiral self-assembly is demonstrated by assembling reconfigurable materials with unique mechanical properties and complex topologies which can easily switch between multiple polymorphic forms[29,30].

Methods Summary: *fd wt* and *fd* Y21M viruses were purified according to previously published protocols[13]. To reduce the number of longer viruses which destabilize monolayer structures such as colloidal membranes or twisted ribbons, virus suspensions were cycled through isotropic-nematic phase coexistence. Only the isotropic portion of the samples, enriched in shorter viruses, was used for experiments[11]. The polydispersity of viruses was quantified using gel electrophoresis (Supplementary Fig. 9). All samples were prepared in a buffer containing 20 mM Tris and 100 mM NaCl at pH=8.0. Addition of the non-adsorbing polymer Dextran (M.W. 500,000, Sigma-Aldrich) induces condensation of rod-like viruses into either flat colloidal membranes or various other chiral assemblages. The strength of chiral interactions between rods was tuned by either changing the sample temperature or by varying the ratio of *fd wt* to *fd* Y21M in membranes containing a mixture of the two viruses[13]. Optical microscopy data was taken with an inverted microscope (Nikon TE-2000) equipped with differential interference contrast (DIC) optics, a homemade heating/cooling stage, and a cooled CCD camera (QImaging, Retiga Exi). The 2D and 3D LC-PolScope imaging setups have been described elsewhere[18,20]. To prevent binding of viruses to surfaces, microscope slides and coverslips were cleaned and subsequently coated with a silane agent (3-(Trimethoxysilyl)propyl methacrylate, Sigma Aldrich) to which a polyacrylamide brush was polymerized from methacrylate groups ensuring that the surfaces did not bind virus particles.

Acknowledgements This work was supported by the National Science Foundation (NSF-MRSEC-0820492, NSF-DMR-0955776, NSF-MRI 0923057) and Petroleum Research Fund (ACS-PRF 50558-DNI7). We acknowledge use of the Brandeis MRSEC optical microscopy facility.

Author Information Reprints and permissions information is available at www.nature.com/reprints. The authors declare no competing financial interests. Readers are welcome to comment on the online version of this article at www.nature.com/nature. Correspondence and requests for materials should be addressed to Zvonimir Dogic (email: zdogic@brandeis.edu)

Author Contributions T.G., E.B., M.J.Z., R.B.M. and Z.D. conceived the experiments and interpreted the results. T.G., E.B., and M.J.Z. performed the experiments. A.W. performed optical trapping experiments.

E.B., C.B. and D.N. performed electron microscopy imaging. M.H. performed experiments on mutant viruses. R.O. performed LC-PolScope imaging. Y.Y and M.F.H. conceived and performed computer simulations. T.G, E.B., M.J.Z., and Z.D. wrote the manuscript.

Figure 1 Edge structure of membranes assembled from an achiral mixture of *fd wt* and *fd* Y21M phages. (**a**) DIC image of a colloidal membrane. (**b**, **c**) Illustration of the colloidal membrane indicating that its edge adopts a surface tension-minimizing curved profile, forcing rods to twist locally. For clarity, the aspect ratio of rods has been reduced. (**d**) Electron micrograph of a membrane directly visualizes the curved edge profile (Supplementary Fig. 3). (**e**) 2D-LC-PolScope birefringence map of two membranes. The bright band associated with the edges indicates local rod tilting (Supplementary Fig. 2). (**f**) 3D-LC-PolScope image composed of an array of conoscopic micro-images, each sampling the local orientation of the rods. In each micro-image, the displacement of the dark spot away from the center determines the local tilting of the rods with respect to the layer normal, the z-axis (Supplementary Fig. 4). (**g-h**) A section of 3D-LC-PolScope images of two edges with clockwise and counterclockwise twist, respectively, illustrating the broken chiral symmetry found at the edge of achiral membranes. (**a, g-h**) Scale bars, 2 μm (**d**) Scale bar, 0.2 μm.

Figure 2. Chiral control of effective line tension γ_{eff}. (**a**) DIC images illustrate the fluctuations of the membrane's edge. Scale bar, 5 μm. (**b**) Fluctuation spectrum ($<a^2_q>$ vs. wavevector q) is plotted for three different temperatures. For small q, $<a^2_q>$ is independent of q and inversely proportional to the effective line tension, $\gamma_{eff} = k_bT/<a^2_q>$. For large q, the suppressed fluctuations are independent of depletant concentration (osmotic pressure) and sample temperature (*fd* chirality) and scale as $1/q^2$. (**c**) γ_{eff} extracted from the low q regime is plotted for a range of sample temperatures (*fd* chirality) and Dextran concentrations (osmotic pressures). In the achiral limit at 60°C, $\gamma_{chiral}=0$ and $\gamma_{bare}=\gamma_{eff}$. Increasing the dextran concentration increases γ_{bare}. Decreasing temperature reduces γ_{eff} due to the increasing γ_{chiral}. (**d**) γ_{chiral} as a function of the twist wave vector q_0 (measured in the cholesteric phase) for various depletant concentrations. The temperature dependence of q_0 is extracted from Supplementary Fig.1. Error bars are s.d.

Figure 3. Transition of a 2D disk into 1D twisted ribbons. (**a**) A temperature quench reduces the line tension, inducing a transition of the 2D membrane into 1D twisted ribbons (Supplementary Movie 1). (**b**) The stability diagram indicates regions of phase space where ribbons and membranes are observed as a function of temperature (chirality) and Dextran concentration. The boundary indicates the temperature above which no stable/metastable ribbons are observed. (**c**) An overlaid phase contrast/fluorescence image of a stable ribbon containing a low volume fraction of fluorescently labeled rods (Supplementary Movie 2). (**d**) LC-PolScope image indicates rod tilting that penetrates from the edge of the ribbon towards its center. (**e**) Schematic structure of twisted ribbons as deduced from optical microscopy. (**f**) A 2D colloidal membrane is trapped with a dual beam optical trap and stretched, inducing the transition to a 1D twisted ribbon (Supplementary Movie 3). The positions of the laser tweezers are marked by the dotted circles. Scale bars, 2 μm.

Figure 4. Hierarchical self-assembly: from isolated viruses and metastable disks to singly and doubly-twisted ribbons. (**a**) In the gray region of the phase diagram in Fig. 3b, *fd* viruses condense into metastable self-limited disks. On longer timescales these disks coalesce and form 1D twisted ribbons. (**b**) Image of a single ribbon which has collapsed into a torroid. **(c)** Doubly-twisted ribbons are assembled from two singly-twisted ribbons with a well-defined phase difference wrapping around each other (Supplementary Fig. 8) (**d**) Directed assembly of a ring-like supramolecular polymer from a linear twisted ribbon using optical tweezers. (**e, f**) A single point mutation of the major coat protein permits microscopic control of ribbon chirality. Wild type *fd* assembles into left handed ribbons whereas the mutant, *fd* Y21M, forms right handed ribbons, as demonstrated by the z-stack series of 2D-LC-PolScope images. Scale bars, 2 μm.

References

1 Pasteur, L. On the relations that can exist between crystalline form, and chemical composition and the sense of rotary polarization. *Ann. Chim. Phys.*, 442 (1848).

2 Hirokawa, N., Tanaka, Y., Okada, Y. & Takeda, S. Nodal flow and the generation of left-right asymmetry. *Cell* 125, 33-45, doi:10.1016/j.cell.2006.03.002 (2006).

3 Harris, A. B., Kamien, R. D. & Lubensky, T. C. Molecular chirality and chiral parameters. *Reviews of Modern Physics* 71, 1745-1757, doi:10.1103/RevModPhys.71.1745 (1999).

4 Oda, R., Huc, I., Schmutz, M., Candau, S. J. & MacKintosh, F. C. Tuning bilayer twist using chiral counterions. *Nature* 399, 566-569, doi:10.1038/21154 (1999).

5 Aggeli, A. *et al.* Hierarchical self-assembly of chiral rod-like molecules as a model for peptide beta-sheet tapes, ribbons, fibrils, and fibers. *Proceedings of the National Academy of Sciences of the United States of America* 98, 11857-11862, doi:10.1073/pnas.191250198 (2001).
6 Kamien, R. D. & Selinger, J. V. Order and frustration in chiral liquid crystals. *Journal of Physics-Condensed Matter* 13, R1-R22, doi:10.1088/0953-8984/13/3/201 (2001).
7 DeGennes, P. G. An anology between superconductors and smectics A *Solid State Communications* 88, 1039-1042, doi:10.1016/0038-1098(93)90291-t (1993).
8 Renn, S. R. & Lubensky, T. C. Abrikosov dislocation lattice in a model of the cholesteric to smectic-A transition. *Physical Review A* 38, 2132-2147, doi:10.1103/PhysRevA.38.2132 (1988).
9 Matsumoto, E. A., Alexander, G. P. & Kamien, R. D. Helical Nanofilaments and the High Chirality Limit of Smectics A. *Physical Review Letters* 103, doi:10.1103/PhysRevLett.103.257804 (2009).
10 Hough, L. E. *et al.* Helical Nanofilament Phases. *Science* 325, 456-460, doi:10.1126/science.1170027 (2009).
11 Barry, E. & Dogic, Z. Entropy driven self-assembly of nonamphiphilic colloidal membranes. *Proceedings of the National Academy of Sciences of the United States of America* 107, 10348-10353, doi:10.1073/pnas.1000406107 (2010).
12 Safran, S. *Statistical Thermodynamics of Surfaces, Interfaces, and Membranes.*, (Addison Wesley, 1994).
13 Barry, E., Beller, D. & Dogic, Z. A model liquid crystalline system based on rodlike viruses with variable chirality and persistence length. *Soft Matter* 5, 2563-2570, doi:10.1039/b822478a (2009).
14 Baumgart, T., Hess, S. T. & Webb, W. W. Imaging coexisting fluid domains in biomembrane models coupling curvature and line tension. *Nature* 425, 821-824, doi:10.1038/nature02013 (2003).
15 Honerkamp-Smith, A. R. *et al.* Line tensions, correlation lengths, and critical exponents in lipid membranes near critical points. *Biophysical Journal* 95, 236-246, doi:10.1529/biophysj.107.128421 (2008).
16 Lee, K. Y. C. & McConnell, H. M. Quantitized symmetry of liquid monolayer domains. *Journal of Physical Chemistry* 97, 9532-9539, doi:10.1021/j100139a044 (1993).
17 Dogic, Z. & Fraden, S. Cholesteric phase in virus suspensions. *Langmuir* 16, 7820-7824, doi:10.1021/la000446t (2000).
18 Oldenbourg, R. & Mei, G. New polarized light microscope with precision universal compensator. *Journal of Microscopy-Oxford* 180, 140-147 (1995).
19 Barry, E., Dogic, Z., Meyer, R. B., Pelcovits, R. A. & Oldenbourg, R. Direct Measurement of the Twist Penetration Length in a Single Smectic A Layer of Colloidal Virus Particles. *Journal of Physical Chemistry B* 113, 3910-3913, doi:10.1021/jp8067377 (2009).
20 Oldenbourg, R. Polarized light field microscopy: an analytical method using a microlens array to simultaneously capture both conoscopic and orthoscopic views of birefringent objects. *Journal of Microscopy-Oxford* 231, 419-432, doi:10.1111/j.1365-2818.2008.02053.x (2008).
21 Aarts, D. G. A. L., Schmidt, M. & Lekkerkerker, H. N. W. Direct visual observation of thermal capillary waves. *Science* 304, 847-850, doi:10.1126/science.1097116 (2004).
22 Fradin, C. *et al.* Reduction in the surface energy of liquid interfaces at short length scales. *Nature* 403, 871-874, doi:10.1038/35002533 (2000).
23 Pelcovits, R. A. & Meyer, R. B. Twist penetration in single-layer smectic A discs of colloidal virus particles. *Liquid Crystals* 36, 1157-1160, doi:10.1080/02678290902921752 (2009).
24 Kaplan, C. N., Tu, H., Pelcovits, R. A. & Meyer, R. B. Theory of depletion-induced phase transition from chiral smectic-A twisted ribbons to semi-infinite flat membranes. *Physical Review E* 82, doi:10.1103/PhysRevE.82.021701 (2010).
25 Srivastava, S. *et al.* Light-Controlled Self-Assembly of Semiconductor Nanoparticles into Twisted Ribbons. *Science* 327, 1355-1359, doi:10.1126/science.1177218 (2010).
26 Chung, W. J. *et al.* Biomimetic self-templating supramolecular structures. *Nature* 478, 364-368, doi:10.1038/nature10513 (2011).
27 Grason, G. M. & Bruinsma, R. F. Chirality and equilibrium biopolymer bundles. *Physical Review Letters* 99, doi:09810110.1103/PhysRevLett.99.098101 (2007).
28 Claessens, M., Semmrich, C., Ramos, L. & Bausch, A. R. Helical twist controls the thickness of F-actin bundles. *Proceedings of the National Academy of Sciences of the United States of America* 105, 8819-8822, doi:10.1073/pnas.0711149105 (2008).

29 Nguyen, T. D. & Glotzer, S. C. Switchable Helical Structures Formed by the Hierarchical Self-Assembly of Laterally Tethered Nanorods. *Small* 5, 2092-2098, doi:10.1002/smll.200900168 (2009).
30 Nguyen, T. D. & Glotzer, S. C. Reconfigurable Assemblies of Shape-Changing Nanorods. *Acs Nano* 4, 2585-2594, doi:10.1021/nn901725b (2010).

Methods

Virus stock solutions. Filamentous viruses were grown using standard biological techniques which have been discussed elsewhere[31]. The resulting virus suspensions contain a low fraction of multimeric virus particles (dimers & trimers) with longer contour lengths. Because high monodispersity in particle length is essential for assembly of membranes and ribbons, the polydispersity was reduced by fractionating the samples through the isotropic-nematic (I-N) phase transition, as longer viruses preferentially dissolve in the nematic liquid crystalline phase. *fd* suspensions (2-8 mL) were prepared at I-N phase coexistence. Only the isotropic (top) portion of the sample, enriched in monomeric viruses was used for subsequent experiments. The fractionation was repeated once or twice in order to obtain sufficiently monodisperse suspensions that reproducibly assemble into colloidal membranes and ribbons. The polydispersity of virus suspensions was quantified using gel electrophoresis of intact viruses. Approximately 20 μl of a 0.5 mg/ml virus solution was loaded into a 1.8% agarose gel and run at 1.4 V/cm for approximately 8 hours[31]. The virus coat protein was dissolved by immersing gels in 0.2M NaOH for 30 minutes, and the remaining DNA was visualized with UV light after staining with Ethidium Bromide (Supplementary Fig. 9)[31]. Only virus suspensions with a monodispersity higher than 95% were used for experiments. For florescence microscopy, viruses were labeled with florescent dyes as described previously[32]. The *fd wt* was labeled with Alexa 488-NHS ester (Invitrogen) and the *fd* Y21M was labeled with DyLight 546-NHS ester (Pierce). All samples were buffered in 20 mM Tris, pH=8.0 to which 100mM NaCl was added to screen electrostatic repulsion between viruses. The concentration of the viruses was determined using absorption spectroscopy[13].

Tuning the twist of the cholesteric phase. The strength of chiral interactions between viruses was quantified by measuring the pitch of a cholesteric liquid crystalline sample. Glass cylindrical capillaries, 0.7 mm in diameter (Charles Supper Company, Natick MA), were filled with *fd* suspensions. In order for the cholesteric texture to properly develop, it was necessary to clean the capillaries in a hot detergent

solution (Hellmanex) after soaking them in 5 M NaOH. After equilibration for several hours, the samples exhibit a well-known fingerprint texture by polarization microscopy that is characteristic of cholesteric liquid crystalline phases (Supplementary Figure 1)[13,17]. The twist wavevector $q_0=2\pi/P$ was determined by measuring the cholesteric pitch *P*. Bulk samples were prepared at 100 mg/ml. Previous work as well as experiments described in Supplementary Figure 4 indicate that this is the effective virus concentration in membranes and ribbons[11]. We assume that q_0 is the same for bulk cholesteric phase and 2D membranes.

Two complimentary methods were used to tune the strength of chiral interactions between *fd* viruses: (i) genetic mutations of the major coat protein and (ii) physical control of sample temperature. Most aspects of the *fd wt* phase behavior, such as the location I-N phase transition, are independent of temperature, as is expected for entropic suspensions of hard rod-like particles, except for a small temperature dependence of the *fd wt* persistence length[33]. Data shown in Supplementary Figure 1 indicates that decreasing temperature increases the strength of chiral interactions between the viruses, as evidenced by the measurements of the cholesteric pitch *P*[17]. Interestingly, the twist wave vector $q_0=2\pi/P$ exhibits evidence of a second order phase transition from a high temperature achiral phase to a low temperature cholesteric phase. In contrast to the temperature dependent chirality of *fd wt*, the chirality of *fd* Y21M does not exhibit any temperature dependence (Supplementary Fig. 6).

An alternative control of chirality involves modifying the composition of the major coat protein. For example, *fd*-Y21M, a mutant that differs from *fd wt* by a single point mutation of the major coat protein, forms a cholesteric helix with the opposite handedness[13]. By controlling the ratio of *fd wt* and *fd* Y21M, it is possible to tune the chirality of the resulting suspension[13]. Such mixtures still form colloidal membranes, and fluorescence microscopy indicates that the two components are uniformly dispersed on resolvable lengthscales (~300 nm). We have used both temperature and genetic methods to tune the chirality of the constituent rods.

Light microscopy sample preparation. Light microscopy chambers were assembled using glass slides and cover slips (Goldseal, Fisher Scientific) with a layer of unstretched parafilm as a spacer. Glass slides

and cover slips were coated with an acrylamide brush to prevent non-specific binding of viruses to the glass surfaces by a procedure described elsewhere[34]. *fd* virus was mixed with the non-adsorbing polymer Dextran (MW 500,000, Sigma-Aldrich) to from membrane and ribbons samples. The virus concentration remained fixed at 10 mg/mL, and the Dextran concentration varied between 30 and 50 mg/mL as indicated in the main text. The samples, sealed using UV-cured glue (Norland Optical) and stored at 4^{o}C, remained good for weeks to months.

Optical microscopy methods. Samples were characterized using a number of complimentary optical microscopy techniques. Except for 3D-LC-PolScope, all observations were made using a 100X oil immersion objective (PlanFluor NA 1.3) on an inverted microscope (Nikon TE-2000). Images were recorded with cooled CCD cameras (CoolSnap HQ, Photometrics or Retiga Exi, QImaging). The microscope was equipped with traditional polarization optics, a Differential Interference Contrast (DIC) module, a fluorescence imaging module and 2D-LC-Polscope microscopy[18]. For 3D-PolScope measurements, we used a Zeiss Axiovert 200M microscope with a Plan Apochomat oil-immersion objective (63X/1.4NA) and a monochrome CCD camera (Retiga 4000R, QImaging)[20].

Sample temperature was tuned between 4 and 60^{o}C with a homemade Peltier module equipped with a proportional integral derivative (PID) temperature controller (ILX Lightwave LPT 5910). The temperature controlling side of the Peltier device was attached to a copper ring fitted to the size of the microscope objective, which heats or cools the sample through the immersion oil. A thermistor, placed in the copper ring adjacent to the sample, permitted the PID feedback necessary to adjust the temperature. Excess heat was removed with constant flow of room temperature water.

3D-LC-PolScope microscopy. Membranes edges with lefthanded and righthanded twist appear indistinguishable when viewed with 2D-LC-PolScope since this technique only provides a 2D projection of the sample birefringence. In order to determine the 3D orientation of rods we used 3D-LC-PolScope microscopy [20]. The 3D-LC-Polscope extends the capabilities of 2D-LC-PolScope by placing a micro-lens array in the image plane of the objective lens. The micro-lens array generates a hybrid image consisting of a series of conoscopic micro-images, each probing a different spatial area in the image plane. Analysis of each conoscopic microimage reveals the local birefringence as a function of the propagation direction

of transmitted light rays. Supplementary Fig. 4a illustrates the path of the optical rays from the specimen plane to the back focal plane of the 3D-LC-PolScope microlens array. Rays shown in green and red pass perpendicularly through the membrane, parallel to its optic axis, and experience no differential retardation. Rays shown in black pass at an angle to the optic axis and are differentially retarded. Rays with the same tilt angle in the specimen plane are focused at the same point in the back focal plane of the objective. The array of microlenses, placed in the image plane of the objective, refocuses these rays into a plane behind the microlens array. Behind each microlens an image of the objectives aperture appears, containing multiple conoscopic images, each specific to rays that have passed through a small region of the specimen. For example, rays emanating from the region *X* of the sample fall onto the microlens *X'*. Therefore, only rays that passed through *X* contribute to the conoscopic image behind *X'*. The same argument applies to rays passing through *Y* and *Y'* and so on.

The conoscopic image of a single microlens focused on the bulk portion of the membrane shows a radially symmetric distribution of the retardance that increases away from the center of the image (Supplementary Fig. 4b). In the center, the rays of light are aligned with the orientation of the viruses and the retardance is zero. Away from the center, the retardance increases because the rays of light become tilted with respect to the orientation of the viruses. When the viruses are tilted with respect to the optical axis, e.g. near the edge of the membrane, the radial profile obtained from a conoscopic image becomes asymmetric and indicates local tilting of the molecules. For colloidal membranes composed of an achiral mixture of *fd wt* and *fd* Y21M, the viruses at the edge of a membrane are found to twist in clockwise and counterclockwise direction with equal probability (Supplementary Fig .4c, 4d and 4e).

Analysis of the 3D-LC-PolScope retardance profile is used to determine the concentration of viruses within a membrane, since the membrane birefringence is proportional to the local rod concentration. It follows that the local retardance of the membrane is given by $R = \Delta n_{sat} dcS \sin^2\theta / \sin\alpha$, where θ is the local tilting of the rods, *c* the concentration of rods within a membrane, *d* is the thickness of the colloidal membrane, *S* is the local order parameter (assumed to be ~ 1), Δn_{sat} is the specific birefringence of a fully aligned bulk sample of *fd* at unit concentration determined by x-ray scattering experiments[35], and α is the orientation of the rays of light as a function of the distance *r* to the center of the conoscopic image given

by $\sin\alpha$ = *(r NA)/(r_{NA}n)* where r_{NA}=*3.9* μm is the size of the conoscopic image, *NA* = 1.4 is the numerical aperture, and *n* = 1.33 is the index of refraction of the solvent. The fitting of this functional form to the retardance profile yields a mean concentration of viruses in the bulk of the membrane of *c*=103±10 mg/mL (Supplementary Fig. 4f). Similar values where obtained with an independent method that involves counting the number of fluorescently labeled particles[11]. Finally, we also note that the concentration of the viruses does not appreciably change with varying Dextran concentration (Supplementary Fig. 4g).

Measurement of the line tension. Line tension was measured by directly imaging and analyzing thermal fluctuations of the membrane's edge with DIC optical microscopy using well established methods[12]. Lower line tension indicates reduced energy required to place the particles at an interface, resulting in larger fluctuations of the membrane's edge. The conformation of the membrane's edge is described by *h(x),* where *x* is the lateral position along the interface and *h(x)* is to local height of the interface. The total length of the interface is:

$$L = \int dx \sqrt{1 + \left(\frac{dh}{dx}\right)^2} \quad (1).$$

For small fluctuations, $\frac{dh}{dx} = \tan\theta \approx \theta$, and the expression for the excess length of the edge compared to a flat interface can be approximated as:

$$\Delta L = \int dx \sqrt{1+\theta^2} - L \approx \frac{1}{2}\int dx \theta^2(x). \quad (2)$$

If line tension γ is the energetic cost per unit length of the edge, the free energy difference between fluctuating and straight edges is given by $\Delta F = \gamma \Delta L$. To make progress, $\theta(x)$ is decomposed into a Fourier series:

$$\theta(x) = \sqrt{\frac{2}{L}} \int_0^L a_q \cos(qx) dx \qquad (3)$$

where *L* is the length of the interface and the wavevector *q* is given by $q=n\pi/L$. The energetic cost of the membrane conformation specified by Fourier amplitudes a_q is given by:

$$\Delta F = \gamma \Delta L = \frac{\gamma}{2}\int_0^L dx \theta^2(x) = \frac{\gamma}{2}\sum_q a_q^2 \quad (4)$$

Invoking the equipartition theorem, it is possible to relate the line tension to fluctuations of the interface:

$$\left\langle a_q^2 \right\rangle = k_B T / \gamma \quad (5)$$

To experimentally measure $\langle a_q^2 \rangle$, we acquired a series of uncorrelated images of the interfacial contour. To ensure optimal contrast, the DIC shear axis was always perpendicular to the membrane's edge. Under these conditions, intensity profile cuts taken perpendicular to the edge could be fit to a Gaussian, yielding the conformation of the edge with sub-pixel accuracy. Each conformation is described in terms of the Fourier amplitudes a_q. Averaging over a sufficient number of uncorrelated images yields a fluctuation spectrum as shown in Fig. 2b, in which the mean square amplitudes $\langle a_q^2 \rangle$ are plotted as a function of wavelength q. In the limit of small q, $\langle a_q^2 \rangle$ is independent of wavenumber as predicted by Eq. 5. With increasing q, the fluctuations are suppressed and scale as q^{-2}. The entire fluctuation spectrum can be quantitatively described by the following equation:

$$\left\langle a_q^2 \right\rangle = \frac{k_B T}{\gamma + \kappa q^2} \quad (6)$$

The $1/q^2$ regime can be obtained by including terms that are proportional to square of the gradient of $\theta(s)$ in Eq. 1. This indicates that there is a bending energy κ associated with fluctuations of the interface, which might be related to the existence of a thin quasi-1D nematic phase located at the edge of the membrane, where the rods are tilted and the layer's smectic ordering is destroyed.

Laser tweezers. Colloidal membranes and ribbons are easily manipulated with optical tweezers. The laser tweezer setup was built around an inverted Nikon TE-2000 microscope. A 1064 nm laser beam (Compass 1064, Coherent) is time-shared between two points via a pair of orthogonally oriented paratellurite (TeO_2) acousto-optic deflectors (AOD, Intra-Action, Bellwood, IL). The laser is projected onto the back focal plane of an oil-immersion objective (Plan Fluor 100X, NA=1.3) and subsequently focused onto the imaging plane. Using custom Labview software, multiple trap locations were specified and used to stretch and manipulate membranes and ribbons.

Electron microscopy methods. For transmission electron microscopy (EM), membranes were assembled as described above with the following differences. The monolayer membranes are relatively small and only stable in solution; therefore, to keep them intact throughout fixation and staining, we

immobilized the membrane assemblies by embedding them in 1% low melting temperature agarose (SeaKem, gelation temperature 25+/- 5^{o}C), in 100mM NaCl, 20mM Tris, pH= 8.15 and 150 mM sucrose as a cryo-protectant. Virus samples were mixed in 1.5 ml eppendorf tubes with fluid agarose at 30^{o}C and kept warm for 3-6 hours to allow formation of relatively large membranes, which was confirmed by light microscopy. Subsequently, a drop of the fluid sample containing membranes was transferred into the 0.1 mm-high cavity of an aluminum planchette for high-pressure freezing (Wohlwend, Switzerland), which was then closed. Then, the sample temperature was decreased to 4^{o}C for 30-45 minutes. The gelled samples were rapidly frozen using a Leica HPM-100 high-pressure freezer (Leica Microsystem, Vienna, Austria). Using a Leica AFS-2 device, the frozen samples were freeze-substituted at low temperatures (starting at -90^{o}C) over the course of 3 days in a solution containing 1% osmium tetroxide (EMS), 0.5% anhydrous glutaraldehyde (EMS) and 2% water in anhydrous acetone (AC32680-0010 Fisher Scientific). After the temperature was raised to 4^{o}C, the sample was infiltrated and embedded in EMbed 812-Resin (EMS). Ultrathin sections of 70 nm thickness were collected on slot grids covered with Formvar support film and post-stained with uranyl acetate (supersaturated solution) and 0.2% lead citrate, before inspection on a FEI Morgan 268 TEM with a 1k CCD camera (GATAN, Inc., Pleasanton, CA) and on a 300 keV Tecnai F30 intermediate voltage TEM (FEI, Inc., Hillsboro, OR) with a 4k CCD camera (GATAN). For electron tomography, we used 150 nm thick sections that were coated with 10 nm colloidal gold particles. Tilt series were recorded over an angular range of +/- 60^{o} with 1^{o} increments on the 300 keV Tecnai F30 TEM using the microscope control software SerialEM[36]. Tomographic reconstructions were calculated with the IMOD software using fiducial alignment and weighted back projection[37].

Computer simulations of the rod/polymer mixture. In the computational model, the rods are represented as hard spherocylinders and the nonadsorbing polymers (depletant) are modeled with ghost spheres, which act as hard spheres when interacting with rods but can freely interpenetrate one another[38]. We performed Metropolis Monte Carlo (MC) with periodic boundary conditions. The system contains 6000 rods in a box with dimensions 140x140x50 (in units of the rod diameter). A constant osmotic pressure is maintained by coupling ghost spheres to a constant chemical potential bath through insertion and deletion moves.The simulations thus sample from the $N_{rod}\mu_{sphere}VT$ ensemble. The rod aspect ratio is 20, the ghost sphere diameter is 1.5 and on average there are about 520 000 spheres.

Simulations were initialized with rods in a monolayer, and Monte Carlo was performed until rod density within the membrane and rod orientations equilibrate. Rods at the membrane edge twist spontaneously regardless of the initial rod orientations in the membrane.

References:

31 Maniatis, T., Sambrook, J. & Fritsch, E. *Molecular Cloning*. (1989).

32 Lettinga, M. P., Barry, E. & Dogic, Z. Self-diffusion of rod-like viruses in the nematic phase. *Europhysics Letters* 71, 692-698, doi:10.1209/epl/i2005-10127-x (2005).

33 Tang, J. X. & Fraden, S. Nonmonotonic temperature dependence of the flexibility of bacteriophage fd. *Biopolymers* 39, 13-22, doi:10.1002/(sici)1097-0282(199607)39:1<13::aid-bip2>3.3.co;2-h (1996).

34 Lau, A. W. C., Prasad, A. & Dogic, Z. Condensation of isolated semi-flexible filaments driven by depletion interactions. *Epl* 87, doi:10.1209/0295-5075/87/48006 (2009).

35 Purdy, K. R. *et al.* Measuring the nematic order of suspensions of colloidal fd virus by x-ray diffraction and optical birefringence. *Physical Review E* 67, doi:10.1103/PhysRevE.67.031708 (2003).

36 Mastronarde, D. N. Automated electron microscope tomography using robust prediction of specimen movements. *Journal of Structural Biology* 152, 36-51, doi:10.1016/j.jsb.2005.07.007 (2005).

37 Kremer, J. R., Mastronarde, D. N. & McIntosh, J. R. Computer visualization of three-dimensional image data using IMOD. *Journal of Structural Biology* 116, 71-76, doi:10.1006/jsbi.1996.0013 (1996).

38 Yang, Y., Barry, E., Dogic, Z. & Hagan, M. F. Self-assembly of 2D membranes from mixtures of hard rods and depleting polymers. *Soft Matter* (2012).

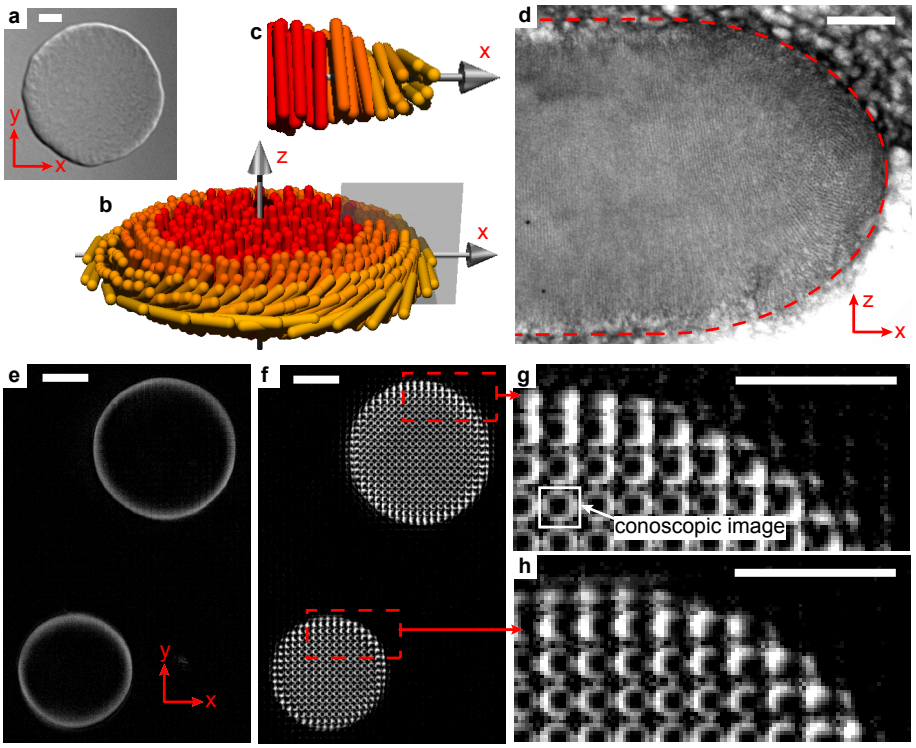
a
y
x
c
x
z
b
x
d
z
x
e
y
x
f
g
conoscopic image
h

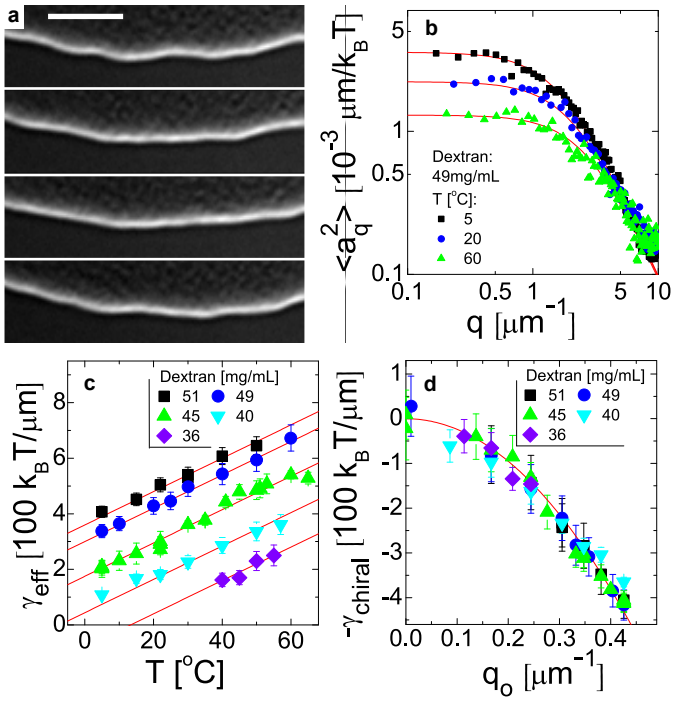
a
b
$\langle a_q^2 \rangle$ [10^{-3} μm/k_BT]
Dextran:
49mg/mL
T [°C]:
5
20
60
q [μm^{-1}]
c
Dextran [mg/mL]
51
49
45
40
36
γ_{eff} [100 k_BT/μm]
T [°C]
d
Dextran [mg/mL]
51
49
45
40
36
-γ_{chiral} [100 k_BT/μm]
q_o [μm^{-1}]

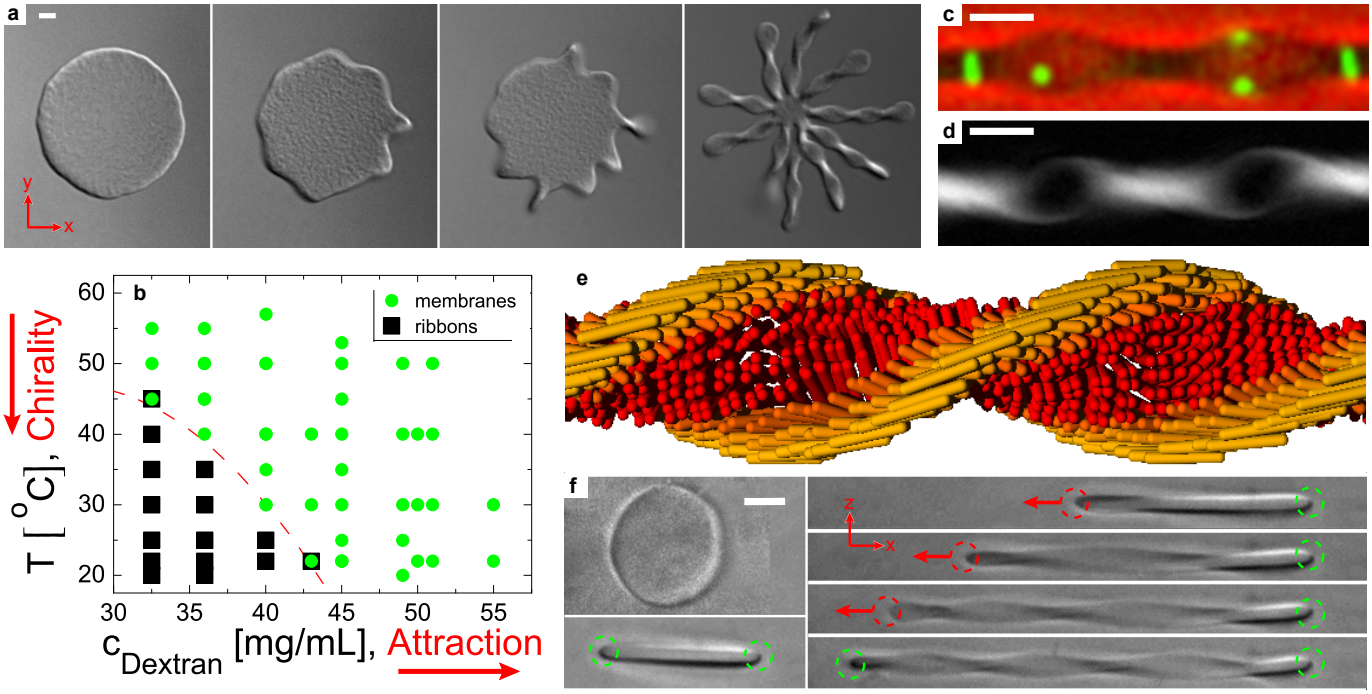
a
y
x
c
d
b
membranes
ribbons
60
50
40
30
20
T [°C], Chirality
30
35
40
45
50
55
c Dextran [mg/mL], Attraction
e
f
z
x

a